Since January 2020 Elsevier has created a COVID-19 resource centre with free information in English and Mandarin on the novel coronavirus COVID-19. The COVID-19 resource centre is hosted on Elsevier Connect, the company's public news and information website.

Elsevier hereby grants permission to make all its COVID-19-related research that is available on the COVID-19 resource centre - including this research content - immediately available in PubMed Central and other publicly funded repositories, such as the WHO COVID database with rights for unrestricted research re-use and analyses in any form or by any means with acknowledgement of the original source. These permissions are granted for free by Elsevier for as long as the COVID-19 resource centre remains active.

Journal of Molecular Liquids 324 (2021) 115134

Contents lists available at ScienceDirect

Journal of Molecular Liquids

journal homepage: www.elsevier.com/locate/molliq

Excited-state electronic properties, structural studies, noncovalent interactions, and inhibition of the novel severe acute respiratory syndrome coronavirus 2 proteins in Ripretinib by first-principle simulations

Fahad A. Alharthi [a], Nabil Al-Zaqri [a,*], Ali Alsalme [a], Afnan Al-Taleb [a], T. Pooventhiran [b], Renjith Thomas [b], D. Jagadeeswara Rao [c]

[a] Department of Chemistry, College of Science, King Saud University, P.O. Box 2455, Riyadh 11451, Saudi Arabia
[b] Department of Chemistry, St. Berchmans College (Autonomous), Changanassery, Kerala, India
[c] Department of Physics, Dr. Lankapalli Bullayya College, Visakhapatnam, Andhra Pradesh, India

ARTICLE INFO

Article history:
Received 8 October 2020
Received in revised form 16 December 2020
Accepted 18 December 2020
Available online 27 December 2020

Keywords:
Ripretinib
Density-functional theory
Time-dependent density-functional theory
Severe acute respiratory novel coronavirus 2
Molecular docking

ABSTRACT

Ripretinib is a recently developed drug for the treatment of adults with advanced gastrointestinal stromal tumors. This paper reports an attempt to study this molecule by electronic modeling and molecular mechanics to determine its composition and other specific chemical features via the density-functional theory (DFT), thereby affording sufficient information on the electronic properties and descriptors that can enable the estimation of its molecular bioactivity. We explored most of the physico-chemical properties of the molecule, as well as its stabilization, via the studies of the natural bond orbitals and noncovalent interactions. The electronic excitation, which is a time-dependent process, was examined by the time-dependent DFT with a CAM-B3LYP functional. The molecular docking study indicated that Ripretinib strongly docks with three known novel severe acute respiratory syndrome coronavirus 2 (SARS-n-CoV-2) proteins with a reasonably good docking score.

© 2020 Elsevier B.V. All rights reserved.

1. Introduction

Gastrointestinal (GI) stromal tumors (GIST) are rare cancers that are associated with the possible metastatic invasion of other body parts, such as lungs, bones, and bone marrow [1]. They are due to the aberrant signaling of the proto-oncogene c-KIT [2,3]. GIST originates from cells that are known as the interstitial cells inside the wall of the GI tract. The interstitial cells are referred to as the GI tract "pacemaker cells" because they are the muscles that contract to push food and liquid along the GI tract. Imatinib, a cancer growth inhibitor called a tyrosine kinase inhibitor, along with the surgical removal of tumors is a gold standard treatment procedure for GIST [4]. Mahadevan demonstrated the resistance to imatinib while applying it to the treatment of cancer and proposed a TK switch to explain the drug resistance [4]. Ripretinib, another kinase inhibitor for treating advanced GIST, was recently developed as an efficient drug to inhibit the entire mutant KIT and PDGFRA kinases that are present in cancers and myeloproliferative neoplasms especially in drug-resistant cases [5]. Employing the structural drug design approach, Flynn and coworkers developed an inhibitor that could bind to the key amino acid residues via the KIT switching mechanism, and it was approved by FDA [6,7] and followed by intense clinical trials [8,9].

Severe acute respiratory syndrome (SARS), which is due to the novel coronavirus 2 (n-CoV-2) (SARS-n-CoV-2) has now emerged to the level of a pandemic that has impacted the lifestyle and health of most people globally [10]. Scientists worldwide are tirelessly working to establish the pathology [11] and epidemiology [11] to develop drugs and vaccines [12]. Chloroquine has been highlighted as a wonder drug for managing the coronavirus disease (COVID) despite the existing differences in opinions [13]. Remdesivir is now presently utilized widely to treat COVID-associated pneumonia [14]. The lopinavir, umifenovir, favipiravir, and oseltamivir molecules are also being studied as potentially active drugs against the virus [15]. Moreover, we have already reported that melatonin is active against this deadly virus [16] along with tucatinib [17] and selpercatinib [18]. Owing to the extensive time that is required to design and develop a drug to treat the virus, it is reasonable to reroute the existing drugs as molecular targets against the virus. Therefore, we considered rimegepant as a potential candidate in this study.

* Corresponding author.
E-mail address: nalzaqri@ksu.edu.sa (N. Al-Zaqri).

https://doi.org/10.1016/j.molliq.2020.115134
0167-7322/© 2020 Elsevier B.V. All rights reserved.

Here, we studied the structural and electronic features of the drug molecule, ripretinib. We employed the density-functional theory (DFT) to study its geometry and electronic and reactivity descriptors. Further, we evaluated the intramolecular electron delocalizations, noncovalent interactions (NCIs), and average local ionization energy indices of the molecule. The most beneficial finding of the study is the potential reuse of the drug as a supplement for the management of SARS-n-CoV-19. The molecular docking of the compound was performed with three known COVID proteins.

2. Methods

The antitumor drug, ripretinib, was optimized by the Gaussian-09 [19] software employing DFT [20] with B3LYP functional [21–23] and a 6-311G + (2 d,p) [24] basis set. We calculated the frequency to ensure that there was no imaginary frequency, thus ensuring that the obtained geometry corresponds to a global minimum for obtaining an optimized geometry. We employed the same geometry to calculate the frontier molecular orbital (FMO), the natural bonding orbitals (NBOs) and to generate the wave function files (.wfn files). To simulate the ultraviolet–visible (UV–Vis) spectrum, we employed the time-dependent DFT (TD-DFT) method [25] with long-range corrected CAM-B3LYP [26,27] functional and 6-311G + (2d,p) as a basis set since the electronic transitions were time-dependent phenomena in a methanol solvent and an Integral Equation Formalism Polarizable Continuum Model (IEFPCM) implicit solvation atmosphere [28,29]. GaussSum was employed to analyze the excited-state electronic transitions and electronic spectra [30]. The ripretinib molecule possesses more than two reaction sites, e.g., the phenylamide, 4-bromo-2-fluorophenyl, methanone, ethyl, methyl, and naphthyridin groups. The reaction sites of ripretinib were calculated by the Multiwavefunction suite employing the generated wfn file [31]. The other energy and reactivity descriptors, including the total electrostatic potential V(r) [23], average localized ionization energy (ALIE), hardness, and softness [32], were determined by the qualitative study of the different NCIs [32]. PDB IDs of the suitable proteins to assess the anti-CoV-2 biological activity of the ripretinib molecule were downloaded from the RCSB [33] site. The energy was obtained from SwissDock, and the score values were obtained from PatchDock [34]. Furthermore, the docked results were obtained from the Bio-discovery studio.

3. Results

3.1. Optimized geometry of ripretinib

The molecular structure of ripretinib was optimized by DFT, and DFT-B3LYP was employed for the structural confirmation with 6-311G + (2d,p) as the basis set. The optimized structure is shown in Fig. 1 and the details of its geometry are presented in Table 1.

The bond angles 1Br–22C–16C, 1Br–22C–24C, 2F–25C–23C, 2F—25C— 24C, 3O–13C–11C, 3O–13C–5 N, 10C–5 N–13C, 13C–5 N–14C, 10C–5 N–14C, 4O—27C, 4O–27C–8 N, 27C–8 N–45H, 27C–8 N–23C, 27C–9 N–49H, 27C–9 N–28C, 29C–28C–30C, 18C–6 N–19C, 6 N–19C–7 N, 19C–7 N–44H, and 19C–7 N–26C were 121.23°, 117.21°, 117.01°, 119.59°, 123.36°, 119.72°, 123.31°, 115.80°, 120.87°, 124.16°, 123.20°, 119.25°, 126.94°, 117.5690°, 128.0°, 119.52°, 117.58°, 115.99°, 118.47°, and 122.91°, respectively. The two halogens were in the meta positions of the middle aromatic ring, thus affording a unique structure.

3.2. FMO properties of ripretinib

FMO offers valuable information about the energy band gap. Thus, the various physical and chemical descriptors of the molecule, which enabled the elucidation of its reactivity, stability, and biological activity, could be predicted by the highest occupied molecular orbital (HOMO) and lowest unoccupied molecular orbital (LUMO) energies [35]. The energies were calculated at the B3LYP/6-311G + (2d,p) level of the theory. The excited states were calculated at the same level by TD-DFT. The frontier energies and other chemical descriptors were related [36,37], and the data are presented in Table 2. HOMO and LUMO were in the 4-bromo-2-fluorophenyl and naphthyridin rings, respectively.

The ground- and excited-state properties are different. The energy gaps in the ground and excited states were 10.12 and 4.05 eV, respectively. This indicates that the excited state was less stable than the ground state, as expected. The free energies of the excited and ground states were − 3.69 and − 2.89 eV, respectively [16,38–40]. The electron-accepting power of the ground state was higher than that in the excited state, whereas the electrodonating power of the excited state is significantly higher than that of the ground state. This may be due to the triplet state of the excited state. Owing to the inherent instability of the excited state, the fraction of the charge that can be transferred is 1.82, and that, which can be transferred in the ground state, is 0.57 only. Therefore, there is increased electrophilicity in the excited state compared to in the ground state [41–44].

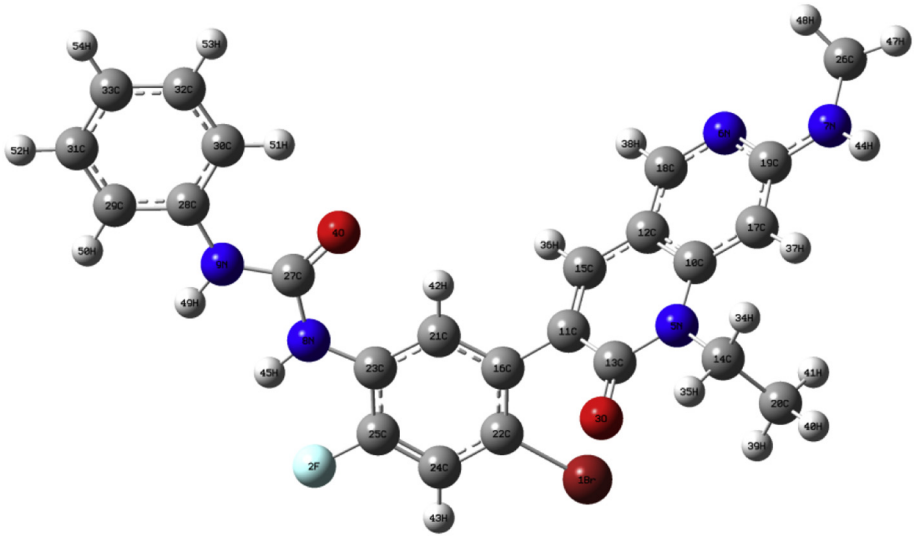

Fig. 1. Optimized structure of ripretinib obtained by DFT (B3LYP/6-311G + (2d,p)) exhibiting the unique structure of the compound with two different halogens in the central ring.

Table 1
Important structural parameters of the molecule (distances and angles).

Name	Definition	Value (in Å)	Name	Definition	Value (in ^{0})
R1	R(1Br—22C)	1.94	A1	A(10C-5 N-13C)	123.31
R2	R(2F—25C)	1.40	A2	A(10C-5 N-14C)	120.88
R3	R(3O—13C)	1.25	A3	A(13C-5 N-14C)	115.81
R4	R(4O—27C)	1.25	A4	A(18C-6 N-19C)	117.59
R5	R(5 N-10C)	1.39	A5	A(19C-7 N-26C)	122.92
R6	R(5 N-13C)	1.42	A6	A(19C-7 N-44H)	118.48
R7	R(5 N-14C)	1.48	A7	A(26C-7 N-44H)	118.61
R8	R(6 N-18C)	1.34	A8	A(23C-8 N-27C)	126.94
R9	R(6 N-19C)	1.37	A9	A(23C-8 N-45H)	113.80
R10	R(7 N-19C)	1.37	A10	A(27C-8 N-45H)	119.26
R11	R(7 N-26C)	1.46	A11	A(27C-9 N-28C)	128.01
R12	R(7 N-44H)	1.01	A12	A(27-9 N-49H)	117.57
R13	R(8 N-23C)	1.41	A13	A(28C-9 N-49H)	114.42
R14	R(8 N-27C)	1.39	A14	A(5 N-10C-12C)	118.39
R15	R(8 N-45H)	1.01	A15	A(5 N-10C-17C)	123.23
R16	R(9 N-27C)	1.39	A16	A(12C-10C-17C)	118.39
R17	R(9 N-28C)	1.42	A17	A(13C-11C-15C)	120.09
R18	R(9 N-49H)	1.01	A18	A(13C-11C-16C)	118.19
R19	R(10C—12C)	1.43	A19	A(15C-11C-16C)	121.66
R20	R(10C—17C)	1.40	A20	A(10C-12C-15C)	119.43
R21	R(11C—13C)	1.47	A21	A(10C-12C-18C)	117.66
R22	R(11C—15C)	1.36	A22	A(15C-12C-18C)	122.90
R23	R(11C—16C)	1.49	A23	A(3O-13C-5 N)	119.72
R24	R(12C—15C)	1.43	A24	A(3O-13C-11C)	123.37
R25	R(12C—18C)	1.41	A25	A(5 N-13C-11C)	116.89
R26	R(14C—20C)	1.53	A26	A(5 N-14C-20C)	112.53
R27	R(14C—34H)	1.09	A27	A(5 N-14C-34H)	108.22
R28	R(14C—35H)	1.09	A28	A(5 N-14C-35H)	105.88
R29	R(15C—36H)	1.09	A29	A(20C-14C-34H)	111.82
R30	R(16C—21C)	1.41	A30	A(20C-14C-35H)	109.79
R31	R(16C—22C)	1.40	A31	A(34H-14C-35H)	108.36
R32	R(17C—19C)	1.41	A32	A(11C-15C-12C)	121.81
R33	R(17C—37H)	1.08	A33	A(11C-15C-36H)	119.84
R34	R(18C—38H)	1.09	A34	A(12C-15C-36H)	118.34
R35	R(20C—39H)	1.09	A35	A(11C-16C-21C)	118.83
R36	R(20C—40H)	1.10	A36	A(11C-16C-22C)	122.59
R37	R(20C—41H)	1.10	A37	A(21C-16C-22C)	118.57
R38	R(21C—23C)	1.40	A38	A(10C-17C-19C)	119.12
R39	R(21C—42H)	1.08	A39	A(10C-17C-37H)	121.53
R40	R(22C—24H)	1.39	A40	A(19C-17C-37H)	119.35
R41	R(23C—25C)	1.40	A41	A(6 N-18C-12C)	124.55
R42	R(24C—25C)	1.38	A42	A(6 N-18C-38H)	116.14
R43	R(24C—43H)	1.08	A43	A(12C-18C-38H)	119.30
R44	R(26C—46H)	1.09	A44	A(6 N-19C-7 N)	115.99
R45	R(26C—47H)	1.09	A45	A(6 N-19C-17C)	122.69
R46	R(26C—48H)	1.09	A46	A(7 N-19C-17C)	121.32
R47	R(28C—29C)	1.41	A47	A(14C-20C-39H)	109.97
R48	R(28C—30C)	1.41	A48	A(14C-20C-40H)	110.02
R49	R(29C—31C)	1.40	A49	A(14C-20C-41H)	111.86
R50	R(29C—50H)	1.09	A50	A(39H-20C-40H)	108.15
R51	R(30C—32C)	1.40	A51	A(39H-20C-41H)	108.42
R52	R(30C—51H)	1.08	A52	A(40H-20C-41H)	108.33
R53	R(31C—33C)	1.40	A53	A(16C-21C-23C)	121.28
R54	R(31C—52H)	1.09	A54	A(16C-21C-42H)	119.93
R55	R(32C—33C)	1.40	A55	A(23C-21C-42H)	118.78
R56	R(32C—53H)	1.09	A56	A(1Br-22C-16C)	121.23
R57	R(33C—54H)	1.08	A57	A(1Br-22C-24C)	117.21
			A58	A(16C-22C-24C)	121.53
			A59	A(8 N-23C-21C)	125.98
			A60	A(8 N-23C-25C)	116.82
			A61	A(21C-23C-25C)	117.19
			A62	A(22C-24C-25C)	118.02
			A63	A(22C-24C-43H)	121.70
			A64	A(25C-24C-43H)	120.28
			A65	A(2F-25C-23C)	117.02
			A66	A(2F-25C-24C)	119.60
			A67	A(23C-25C-24C)	123.39
			A68	A(7 N-26C-46H)	111.25
			A69	A(7 N-26C-47H)	108.37
			A70	A(7 N-26C-48H)	111.30
			A71	A(46H-26C-47H)	109.16
			A72	A(46H-26C-48H)	107.57
			A73	A(47H-26C-48H)	109.16
			A74	A(4O-27C-8 N)	123.21

(continued on next page)

Table 1 (*continued*)

Name	Definition	Value (in Å)	Name	Definition	Value (in ^{0})
			A75	A(4O-27C-9 N)	124.17
			A76	A(8 N-27C-9 N)	112.62
			A77	A(9 N-28C-29C)	116.83
			A78	A(9 N-28C-30C)	123.65
			A79	A(29C-28C-30C)	119.52
			A80	A(28C-29C-31C)	120.48
			A81	A(28C-29C-50H)	119.74
			A82	A(31C-29C-50H)	119.78
			A83	A(28C-30C-32C)	119.26
			A84	A(28C-30C-51H)	119.58
			A85	A(32C-30C-51H)	121.15
			A86	A(29C-31C-33C)	120.24
			A87	A(29C-31C-52H)	119.45
			A88	A(33C-31C-52H)	120.31
			A89	A(30C-32C-33C)	121.35
			A90	A(30C-32C-53H)	118.75
			A91	A(33C-32C-53H)	119.90
			A92	A(31C-33C-32C)	119.16
			A93	A(31C-33C-54H)	120.36
			A94	A(32C-33C-54H)	120.48

Table 2
Ground- and excited-state energies of the molecule calculated at the B3LYP/6311 + (2d,p) level to describe the various chemical reactivity descriptors.

	Ground State	Excited State
HOMO	−7.92	−5.71
LUMO	2.20	−1.66
Energy gap, ΔE	10.12	4.05
Ionization energy (I = εHOMO = –HOMO)	7.92	5.71
Electron affinity (A = εLUMO = –LUMO)	−2.20	1.66
Global hardness (η = (I − A)/2)	5.06	2.03
Global softness (S = 1/η)	0.20	0.49
Chemical potential (μ = −(I + A)/2)	−2.86	−3.69
Electronegativity (χ = −μ)	2.86	3.69
Electrophilicity index (ω = μ2/2η)	0.81	3.35
Nucleophilicity index (*N* = 1/ω)	1.24	0.30
ΔN_{max}	0.57	1.82
Electroaccepting power, ω + = A2/2(I − A)	0.24	0.34
Electrodonating power ω + = I2/2(I − A)	−4.32	−44.27

3.3. Electronic spectra of the compound and light-harvesting efficiency

The electronic transition of ripretinib was studied by TD-DFT utilizing CAM-B3LYP functional and 6-311G + (2d,p) as the basis set in a methanol implicit solvent atmosphere employing the IEFPCM solvation model. The UV–Vis spectrum and the different orbitals involved in the transition are given in Figs.2 and 3, respectively.

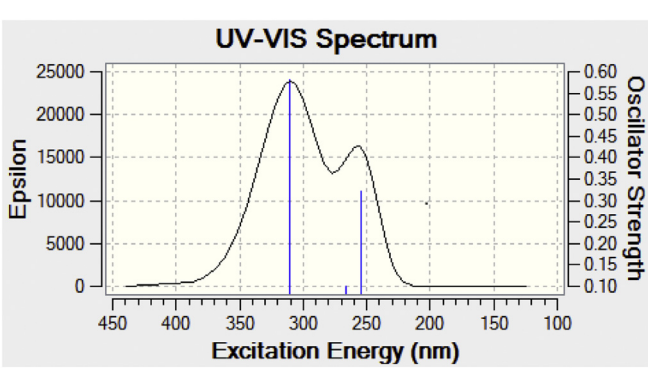

Fig. 2. Simulated UV–Vis spectrum of ripretinib by TD-DFT/CAM-B3LYP/6–311 + G(2d,p) in methanol employing the IEFPCM model and exhibiting two distinct UV absorptions.

There are two prominent electronic transitions of the compound. The energy, wavelength, oscillator strength (f), and symmetry of the first transition are 32,154.32 cm^{-1}, 311.00 nm, 0.58, and singlet asymmetry, respectively. The major contributions to these transitions (91%) are from HOMO to LUMO. HOMO is in the 4-bromo-2-fluorophenyl ring, and LUMO is in the naphthyridn one. Hence, the HOMO–LUMO transition involves electromigration from one region of the molecule to another, thereby inducing an intramolecular charge-transfer process. Regarding the second transition, the energy, wavelength, f, and symmetry are 39,373.03 cm^{-1}, 253 nm, 0.32, and singlet asymmetry, respectively, with major contributions from the seventh lowest HOMO (HOMO-7) to LUMO, the second HOMO (HOMO-2) to LUMO, and HOMO to the second LUMO (LUMO +2) with 26%, 27%, and 13% contributions, respectively.

For the first transition, *f* was 0.58, which implies that the molecule possessed good light-harvesting efficiency (LHE) that is expressed as a function of *f*, as follows: LHE = $1–10^{-f}$ [36,45–50]. The value was 0.7376 for the first transition, which indicated that the compound could absorb 73.76% of incident-light energy for electronic excitation at that wavelength.

3.4. NLO properties of ripretinib

The study of light–matter interactions is very beneficial, especially for organic molecules. The ability of the molecule to bend the linear light can be determined by the polarizability and hyperpolarizability values, which were obtained from the simulation of the Raman spectra. These NLO activities are very beneficial to employing the compound in the organic electronics industry [51–54]. The polarizability and hyperpolarizability data that were obtained during the simulation of Raman spectra were utilized for the estimation. The simulation was conducted at the same theoretical level as that of the optimization and compared with those of the standard NLO-active substance, urea [55–57]. The parameters of the NLO properties of ripretinib are shown in Table 3.

The dipole moment (μ), mean polarizability (α_0), the anisotropy of the polarizability (Δα), and molar refractivity (MR) of ripretinib are 0.9804 D, 341.3780*10^{-23} esu, 795.2260*10^{-23} esu, and 8614. 8331 esu, respectively, which are 3.1091 times lower than urea, 9.5752 times higher than urea, 11.5122 times higher than urea, and 9.5752 times higher than urea, respectively, when compared against those of the standard, urea. Thus, this molecule exhibits higher NLO properties than urea.

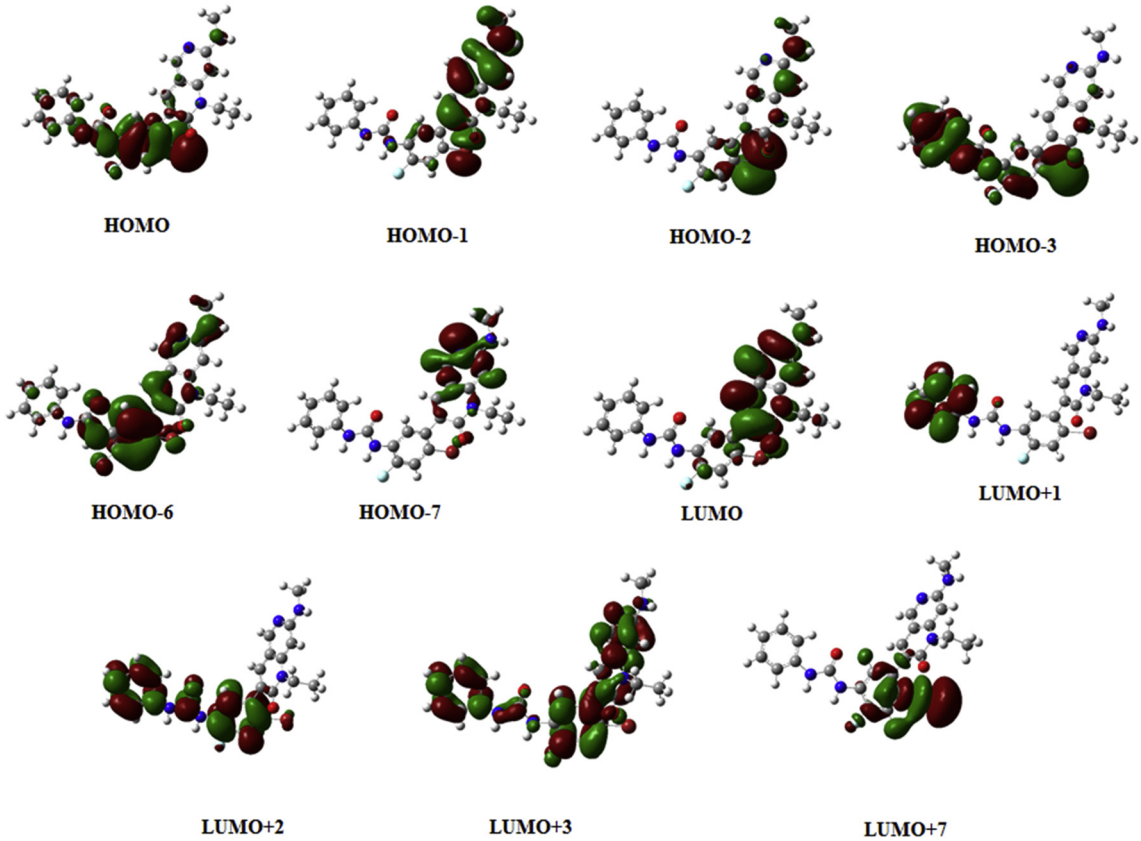

Fig. 3. Pictorial representation of the various MOs involved in the electronic transitions. HOMO is in the central ring, while LUMO is delocalized over the naphthydrin group.

3.5. NBO of ripretinib

Intramolecular electron displacements are very essential because they determine the inherent stability of a compound. The NBO analysis is an excellent tool for studying such interactions via hyperconjugations [58–61]. The occupancy values of NBOs and their delocalization energy avails valuable information on the aforementioned stabilities. NBOs were calculated with the NBO suite [62] that is available on the Gaussian-09 software.

Table 4 summarizes the delocalization energy during the electronic transitions. The electrons are transferred from the donor bonding orbitals to the acceptor antibonding orbitals with suitable occupancies utilizing energy, i.e., from σ (N6–C18) with an occupancy of 1.7872 to σ* (C10–C12) and σ* (C17–C19) with energies of 10.35 and 26.82 kcal/mol, respectively; from σ (C10–C12) with an occupancy of 1.5410 to σ* (N6–C18), σ* (C11–C15), and σ* (C17–C19) with energies of 33.68, 19.50, and 14.63 kcal/mol, respectively; from σ (C11–C15) with an occupancy of 1.7933 to σ* (O3–C13) and σ* (C10–C12) with energies of 25.98 and 12.56 kcal/mol, respectively; from σ (C17–C19) with an occupancy of 1.6378 to σ* (N6–C18) and σ* (C10–C12) with energies of 12.00 and 29.59 kcal/mol respectively; from σ (C22–C24) with an occupancy of 1.6861 to σ* (C16–C21) and σ* (C23–C25) with energies of 21.63 and 20.68 kcal/mol, respectively; from σ (C23–C25) with an occupancy of 1.6521 to σ* (C16–C21) and σ* (C22–C24) with energies of 18.32 and 23.88 kcal/mol, respectively; from σ (C28–C30) with an occupancy of 1.6392 to σ* (C29–C31) and σ* (C32–C33) with energies of 19.85 and 18.45 kcal/mol, respectively; from σ (C29–C31) with an occupancy of 1.7001 to σ* (C28–C30) and σ* (C32–C33) with energies of 21.93 and 18.45 kcal/mol, respectively; and from σ (C32–C33) with an occupancy of 1.6651 to σ* (C28–C30) and σ* (C29–C31) with energies of 20.55 and 24.06 kcal/mol, respectively.

The lone pairs of electrons were transferred from the bonding orbitals to the antibonding lone pairs of the antibonding orbitals, i.e., from the lone pair orbitals, n(F2), n (O4), and n(N7), with occupancies of 1.9463, 1.5404, and 1.7224, respectively, to the antibonding orbitals, σ* (C23–C25), n* (C27), and σ* (C17–C19), with energies of 13.01, 286.47, and 51.50 kcal/mol, respectively; from n (O3) with an occupancy of 1.8789 to σ* (N5–C13) and σ* (C11–C13) with energies of 25.50 and 15.65 kcal/mol, respectively; from n (O4) with an occupancy of 1.8708 to σ* (N8–C27) and σ* (N9–C27) with energies of 22.19 and 21.82 kcal/mol, respectively; from n (N5) with an occupancy of 1.5969 to σ* (O3–C13) and σ* (C10–C12) with energies of 54.25 and

Table 3
NLO properties of ripretinib compared with those of a standard material (urea). The polarizability and hyperpolarizability data from the Raman simulation were utilized for their calculations.

Nonlinear property	Ripretinib	Urea	Comparison with urea
Dipolemoment (μ)	0.9804 D	3.0482 D	3.1091 times lower
Mean polarizability (α_0)	$341.3780*10^{-23}$ esu	$35.6521*10^{-23}$ esu	9.5752 times higher
Anisotropy of the polarizability (Δα)	$795.2260*10^{-23}$ esu	$69.0764*10^{-23}$ esu	11.5122 times higher
Molar Refractivity (MR)	8614.8331 esu	899.6973 esu	9.5752 times higher

Table 4
Estimnated delocalization energy for different electronic trasitioms delocalisations in the molecule.

NBOs	Donor NBO (i)	NBOs	Acceptor NBO (j)	Energy (in kcal/mol)	Occupancy
10	BD [2] N6-C18	292	BD* [2] C10-C12	10.35	1.79
10	BD [2] N6-C18	308	BD* [2] C17-C19	26.82	1.79
22	BD [2] C10-C12	280	BD* [2] N6-C18	33.68	1.54
22	BD [2] C10-C12	296	BD* [2] C11-C15	19.50	1.54
22	BD [2] C10-C12	308	BD* [2] C17-C19	14.63	1.54
26	BD [2] C11-C15	274	BD* [2] O3-C13	25.98	1.79
26	BD [2] C11-C15	292	BD* [2] C10-C12	12.56	1.79
38	BD [2] C17-C19	280	BD* [2] N6-C18	12.00	1.64
38	BD [2] C17-C19	292	BD* [2] C10-C12	29.59	1.64
47	BD [2] C22-C24	305	BD* [2] C16-C21	21.63	1.69
47	BD [2] C22-C24	319	BD* [2] C23-C25	20.68	1.69
49	BD [2] C23-C25	305	BD* [2] C16-C21	18.32	1.65
49	BD [2] C23-C25	317	BD* [2] C22-C24	23.88	1.65
57	BD [2] C28-C30	329	BD* [2] C29-C31	19.85	1.64
57	BD [2] C28-C30	336	BD* [2] C32-C33	22.37	1.64
59	BD [2] C29-C31	327	BD* [2] C28-C30	21.93	1.70
59	BD [2] C29-C31	336	BD* [2] C32-C33	18.45	1.70
66	BD [2] C32-C33	327	BD* [2] C28-C30	20.55	1.67
66	BD [2] C32-C33	329	BD* [2] C29-C31	24.06	1.67
106	LP [3] F2	319	BD* [2] C23-C25	13.01	1.95
108	LP [2] O3	277	BD* [1] N5-C13	25.50	1.88
108	LP [2] O3	294	BD* [1] C11-C13	15.65	1.88
110	LP [2] O4	286	BD* [1] N8-C27	22.19	1.87
110	LP [2] O4	288	BD* [1] N9-C27	21.82	1.87
110	LP [2] O4	315	BD* [1] C21-H42	1.49	1.54
111	LP [3] O4	117	LP* [1] C27	286.47	1.54
112	LP [1] N5	274	BD* [2] O3-C13	54.25	1.60
112	LP [1] N5	292	BD* [2] C10-C12	44.45	1.60
114	LP [1] N7	308	BD* [2] C17-C19	51.50	1.72
115	LP [1] N8	117	LP* [1] C27	106.55	1.70
115	LP [1] N8	319	BD* [2] C23-C25	34.35	1.70
116	LP [1] N9	117	LP* [1] C27	114.22	1.70
116	LP [1] N9	327	BD* [2] C28-C30	31.82	1.70
274	BD* [2] O3-C13	296	BD* [2] C11-C15	50.01	0.37
280	BD* [2] N6-C18	292	BD* [2] C10-C12	255.94	0.37
280	BD* [2] N6-C18	308	BD* [2] C17-C19	242.87	0.37
292	BD* [2] C10-C12	296	BD* [2] C11-C15	117.36	0.51
317	BD* [2] C22-C24	305	BD* [2] C16-C21	184.42	0.41
319	BD* [2] C23-C25	305	BD* [2] C16-C21	122.92	0.45
319	BD* [2] C23-C25	317	BD* [2] C22-C24	385.89	0.45

44.45 kcal/mol, respectively; from n (N6) with an occupancy of 1.9150 to σ* (C12–C18) and σ* (C17–C19) with energies of 11.42 and 11.03, respectively; from n (N8) with an occupancy of 1.7035 to n* (C27) and σ* (C23–C25) with energies of 106.55 and 34.35 kcal/mol, respectively; and from n (N9) with an occupancy of 1.7000 to n* (C27) and σ* (C28–C30) with energies of 114.22 and 31.82 kcal/mol, respectively.

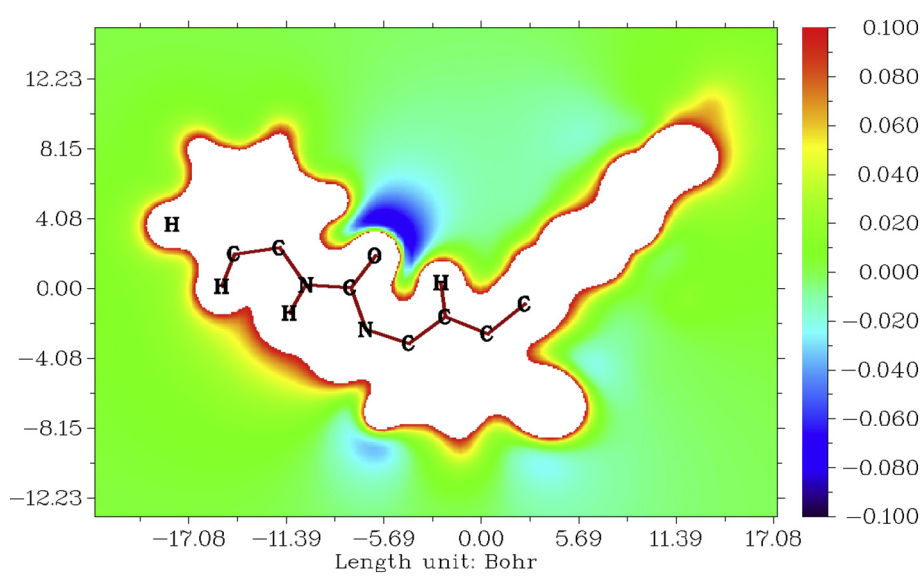

Fig. 4. MESP map of ripretinib indicating the surface-charge distribution contour.

3.6. Molecular electrostatic potentials (MESP) map of ripretinib

The electrostatic potential, V(r), which is generated around a molecule by its nuclei and electrons and treated as static charge distribution, is a very beneficial property for studying and predicting molecular reactivity. This is narrowly defined and can be calculated experimentally and computationally. The capacity has been especially essential in indicating the positions or regions of the molecule where the advancing electrophile is initially drawn and has also been effectively extended to analyzing the associations that require a certain optimal relative orientation of the reactants, such as between the product and its cellular receptor [35,63,64]. MESP of the ripretinib molecule was generated from the data that was obtained from the previous calculation (Fig. 4).

The blue and red colors correspond to the numerical values between −0.1000 and 0.1000 and the molecule in the Bohr^3 range of 17.08 to −22.50. The blue color corresponds to the oxygen atom (the electrophilic region) in the amide group, the fluorine atom in the phenyl ring, and the ketonic oxygen atom in the naphthyridin group, which are the electron-rich sites, indicating that the electrophiles could easily attack these sites. The red color corresponds to all the protons in the amide group (the nucleophilic region), bromine atom in the phenyl group, and all the protons in the methylamine group, which are electron-poor sites, indicating that nucleophiles can easily attack these sites.

3.7. ALIE property of ripretinib

The local, I(r), average ionization energy of ionization is the energy that is required to remove an electron from point r into the system. The lowest values represent the positions of the least tightly held electrons, which are, therefore, the selected reaction sites with electrophiles or radicals. Beyond its relevance to the reactive behavior, I(r) is significant in other fundamental fields, including atomic shell composition, electronegativity, and local polarizability and hardness [65]. ALIE of ripretinib is pictorially shown in Fig. 5.

A color code can be employed to identify the ALIE surface of the molecule. The average volume of the molecule is in the −17.17 to −17.17 Bohr^3 range. The bluish-green region indicates the delocalization of the electrons in the phenyl group, in the amide chain, from fluorine to the 4-bromo-2-fluorophenyl group, in the naphthyridin group, and in the methylamino chain, which produced several resonance structures that stabilized the molecule. The blue color indicates the sigma-bond, as well as the stable bond between the atoms in the ripretinib molecule, which are the protons to be attached to the methyl, ethyl, naphthyridin, and phenyl groups.

3.8. NCI property of ripretinib

NCI differs from a covalent bond because it does not involve the sharing of electrons, although it involves more dispersed variations of the electromagnetic interactions between the molecules or within a molecule. The three-dimensional arrangement of large molecules, such as proteins and nucleic acids, is crucial to NCI. Additionally, it is involved in many biological processes where large molecules bind to each other specifically but transiently. These interactions also significantly impact drug design, crystallinity and material design, self-assembling, and the design of the synthesis of tailored organic molecules [44]. The molecular structure of ripretinib was optimized and the multiwfn file was generated by DFT employing DFT-B3LYP as a method and 6-311G + (2d,p) as a basic set. NCI of ripretinib is shown in Fig. 6.

A graph of energy against the reduced density gradient was plotted. The hydrogen bond appeared between −0.005 and − 0.021 a.u. from the hydrogen atoms in the amide nitrogen and the phenyl fluorine atom in the 4-bromo-2-fluorophenyl group. The van der Waals force attraction was observed in the range of −0.005 to 0.008 a.u. from the protons in the phenyl group to the amide oxygen and from the protons in the naphthyridin group to the ketonic oxygen. The steric force exists in the range of 0.008–0.25 a.u. involving the bromine atom in the 4-bromo-2-fluorophenyl group and the ethyl group in the naphthyridin group. All these interactions stabilized the system and ensured its reactivity toward biological systems.

3.9. Molecular docking

Scientists globally are researching drugs to manage the COVID pandemic. It is generally preferable to reroute existing drugs during this pandemic to save a lot of precious time that is required for new drug discovery. Therefore, we evaluated the activity of this drug against known COVID proteins. Molecular docking explains the structure-related activity of ripretinib against coV-2 proteins (PDB IDs:6M03 [66], 6 W63 [1], and 6 LU7 [1]) that have been deposited in the RSC database [33]. Table 5 explains the docking result between ripretinib and the coV-2

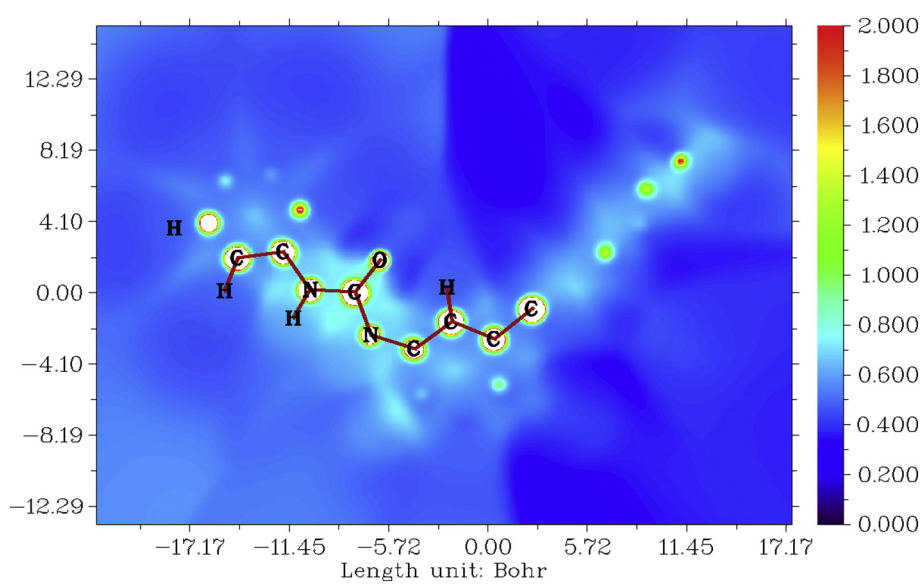

Fig. 5. ALIE of the ripretinib molecule.

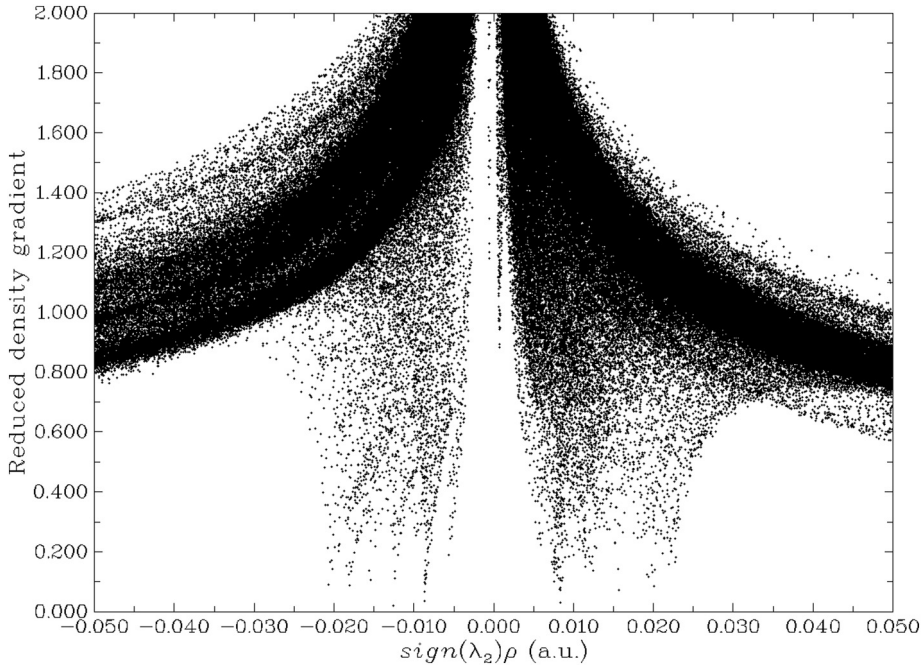

Fig. 6. Graph of NCI against the reduced density gradient and interaction energy.

proteins (PDB IDs: 6M03, 6W63, and 6LU7), as follows: the 6 M03 protein possessed the highest inter-full fitness, ΔG ligand–solvent polarity, and total ΔG among the proteins. The 6 W63 protein possessed the highest surface-full fitness, ΔG complex–solvent nonpolarity, and ΔG protein–solvent nonpolarity among the proteins. Further, the 6 LU7 protein possessed the highest energy, simple fitness, full fitness, intra-full fitness, solvent-full fitness, ΔG complex–solvent polarity, ΔG protein–solvent polarity, and ΔG ligand–solvent nonpolarity among the proteins.

Ripretinib against the coV-2 proteins (6 M03, 6 W63, and 6 LU7) obtained the respective score values of 5242, 5328, and 5780; interaction areas of 578.70, 658.40, and 634.60; and minimum atomic contact energies of −192.77, −270.60, and − 288.10.

Fig. 7 shows the skeletal structure of the interactions between ripretinib and the 6 M03, 6 W63, and 6 LU7 proteins. Fig.S1 shows the interactions between ripretinib and the 6 M03, 6 W63, and 6 LU7 residues, and Table S1 presents the interactions of ripretinib with 6 M03, 6 W63, and 6 LU7. All the names of the protein residues and their labels, hydrophobicity, pKa values, average isotropic displacements, secondary structures, residue solvent accessibility, sidechain solvent accessibility, percentage solvent accessibility, and the percentage sidechain solvent accessibility values for interactions with ripretinib are presented in the table.

Table S2 presents the nonbond interactions between ripretinib and the 6 M03, 6 W63, and 6 LU7 proteins with the distance, category, type, from chemistry, and to the chemistry of the favorable, unfavorable nonbond, and unsatisfied bonds within the ripretinib molecule.

Table 6 and Figs. S2, S3, S4, S5, and S6 show the noncovalent bonds between ripretinib and the coV-2 proteins (6 M03, 6 W63, and 6 LU7) and explain the hydrophobicity, hydrophilicity, neutral group-, acidic group-, and basic-group interactions, respectively.

4. Conclusions

We studied the structural features, energy features, energy descriptors, and other beneficial physical properties of ripretinib.

Table 5
Docking results of ripretinib with coV-2 proteins.

Parameters	6 M03	6 W63	6 LU7
Energy	26.1878 kcal/mol	25.2982 kcal/mol	26.4866 kcal/mol
Simple Fitness	26.1878 kcal/mol	25.2982 kcal/mol	26.4866 kcal/mol
Full Fitness	−1214.3522 kcal/mol	−1206.2007 kcal/mol	−1243.4666 kcal/mol
Inter-Full Fitness	−59.9006 kcal/mol	−47.326 kcal/mol	−41.9352 kcal/mol
Intra-Full Fitness	−4.05057 kcal/mol	−8.21465 kcal/mol	−8.64033 kcal/mol
Solvent-Full Fitness	−1368.99 kcal/mol	−1370.48 kcal/mol	−1411.76 kcal/mol
Surface-Full Fitness	218.589 kcal/mol	219.82 kcal/mol	218.869 kcal/mol
Extra-Full Fitness	0 kcal/mol	0 kcal/mol	0 kcal/mol
ΔG complex–solvent polarity	−1368.99 kcal/mol	−1370.48 kcal/mol	−1411.76 kcal/mol
ΔG complex–solvent nonpolarity	218.589 kcal/mol	219.82 kcal/mol	218.869 kcal/mol
ΔG protein–solvent polarity	−1385.67 kcal/mol	−1372.14 kcal/mol	−1411.41 kcal/mol
ΔG protein–solvent nonpolarity	221.3 kcal/mol	222.123 kcal/mol	221.095 kcal/mol
ΔG ligand–solvent polarity	−17.5824 kcal/mol	−15.3128 kcal/mol	−16.6198 kcal/mol
ΔG ligand–solvent nonpolarity	8.95781 kcal/mol	9.10841 kcal/mol	9.12255 kcal/mol
ΔG van der Waals force	−59.9006 kcal/mol	−47.326 kcal/mol	−41.9352 kcal/mol
ΔG electric force	0 kcal/mol	0 kcal/mol	0 kcal/mol
Total ΔG	−8.66 kcal/mol	−8.50 kcal/mol	−8.03 kcal/mol

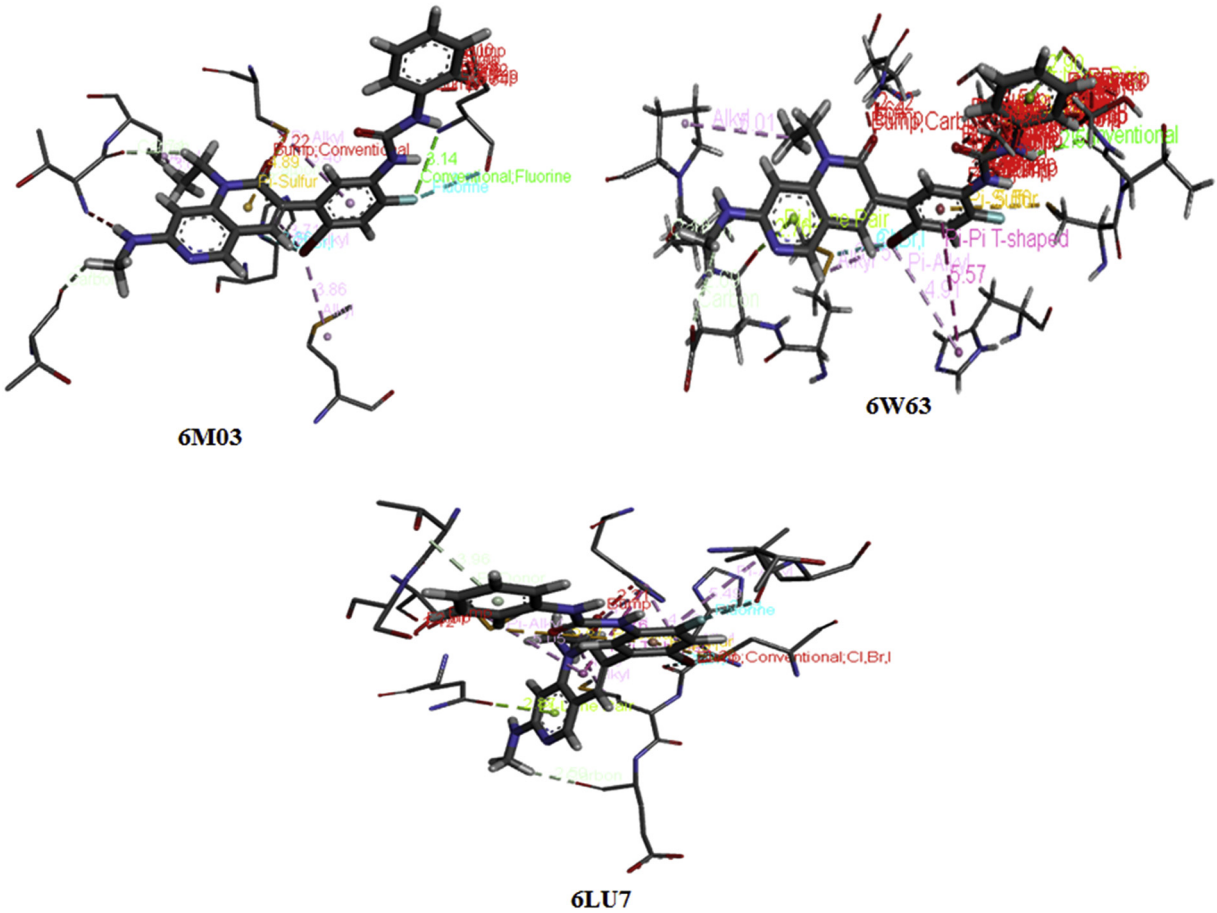

Fig. 7. Skeletal structures of the interactions between ripretinib and the 6 M03, 6 W63, and 6 LU7 proteins.

Table 6
Nonbond interaction labels between the coV-2 protein residues and ripretinib.

Nonbond interactions	Names of the coV-2 proteins	Labels of the coV-2 proteins
Hydrophobicity	6 M03	THR A:24, THR A:26, LEU A:27, HIS A:41, VAL A:42, MET A:49, PHE A:140, LEU A:141, CYS A:145, MET A:165, and GLU A:166
	6 W63	HIS A:41, CYS A:44, THR A:45, SER A:46, MET A:49, MET A:165, GLU A:166, LEU A:167, PRO A:168, and GLN A:189
	6 LU7	THR A:26, LEU A:27, HIS A:41, THR A:45, SER A:46, MET A:49, CYS A:145, HIS A:164, MET A:165, GLU A:166, and GLN A:189
Hydrophilicity	6 M03	THR A:24, THR A:26, HIS A:41, ASN A:142, GLU A:166, and GLN A:189
	6 W63	HIS A:41, THR A:45, SER A:46, GLU A:47, ASP A:48, GLU A:166, PRO A:168, ASP A:187, ARG A:188, GLN A:189, and GLN A:192
	6 LU7	THR A:26, HIS A:41, THR A:45, SER A:46, HIS A:164, GLN A166, ASP A:187, ARG A:188, and GLN A:189
Neutral group	6 M03	THR A:24, THR A:25, THR A:26, SER A:46, GLY A:143, and GLY A:170
	6 W63	THR A:45, SER A:46, TYR A:54, PRO A:168, GLY A:170, and THR A:190
	6 LU7	THR A:24, THR A:25, THR A:26, THR A:45, SER A:46, TYR A:54, and GLY A:143
Acidic groups	6 M03	THR A:24, THR A:26, and GLU A:166
	6 W63	GLU A:47, ASP A:48, GLU A:166, and ASP A:187
	6 LU7	GLU A:187 and ASP A:187
Basic groups	6 M03	THR A:24, THR A:26, and HIS A:41
	6 W63	HIS A:41 and ARG A:188
	6 LU7	HIS A:41, HIS A:164, and ARG A:188

The UV–Vis spectra exhibit a significant peak at 311 nm with f of 0.5812. From the NLO property of ripretinib, the mean polarizability and anisotropy of the polarizability are 9.5752 and 11.5122 times greater than those of the standard material, urea. The stability and intramolecular-charge delocalization were studied employing NBO. The properties of the reactive site, such as MESP, ALIE, and NCI, were detailedly explained, and it was confirmed that they occurred mostly in the amide oxygen, nitrogen, and protons in the phenylamide group; the fluorine and bromine and protons in the 4-bromo-2-fluorophenyl group; and the ketonic oxygen, methylamino, and ethyl protons in the naphthyridin group. Most significantly, the docking studies indicate that the molecule docks extensively with three important docking proteins (6 M03, 6 W63, and 6 LU7) that are related to CoV-2. Hence, this compound should be studied as a possible drug against SARS-n-CoV-2. ΔGs of the dockings of 6 M03, 6 W63, and 6 LU7 are − 8.66, 8.50, and − 8.03 kcal/mol, respectively, which are appreciable values. Thus, this compound could be developed as a drug to treat CoV-2 after screening via biological studies.

Credit authorship contribution statement

Fahad A. Alharthi : Simulation, data curation, writing original draft; **Nabil Al Zaqri** : Experiment design, Fund acquisition, Supervision; **Ali Alsalme**: Writing, reviewing and editing, Validation, Data analysis; **Afnan Al-Taleb** : Simulations, Validation; T. Pooventhiran.: Investigation, Simulation, Data curation, Writing- original drafts, Writing- revised draft; **Renjith Thomas**: Conceptualization,

Methodology, Software, Supervision; **D.J Rao**: Simulations, Validation, Formal analysis.

Declaration of Competing Interest

Authors declare no conflicts of interest.

Acknowledgment

The authors extend their appreciation to the Deputyship for Research & Innovation, "Ministry of Education" in Saudi Arabia for funding this research work through the project number IFKSURG- 1440-141.

Appendix A. Supplementary data

Supplementary data to this article can be found online at https://doi.org/10.1016/j.molliq.2020.115134.

References

[1] A.D. Mesecar, RCSB PDB - 6W63: Structure of COVID-19 Main Protease Bound to Potent Broad-Spectrum Non-covalent Inhibitor X77, RCSB, 2020https://doi.org/10.2210/pdb6W63/pdb.
[2] J.G. Kettle, R. Anjum, E. Barry, D. Bhavsar, C. Brown, S. Boyd, A. Campbell, K. Goldberg, M. Grondine, S. Guichard, C.J. Hardy, T. Hunt, R.D.O. Jones, X. Li, O. Moleva, D. Ogg, R.C. Overman, M.J. Packer, S. Pearson, M. Schimpl, W. Shao, A. Smith, J.M. Smith, D. Stead, S. Stokes, M. Tucker, Y. Ye, Discovery of N-(4-{[5-Fluoro-7-(2-methoxyethoxy)quinazolin-4-yl]amino}phenyl)-2-[4-(propan-2-yl)-1H-1,2,3-triazol-1-yl]acetamide (AZD3229), a Potent Pan-KIT mutant inhibitor for the treatment of gastrointestinal stromal tumors, J. Med. Chem. 61 (2018) 8797–8810, https://doi.org/10.1021/acs.jmedchem.8b00938.
[3] T. Doi, Y. Kurokawa, A. Sawaki, Y. Komatsu, M. Ozaka, T. Takahashi, Y. Naito, S. Ohkubo, T. Nishida, Efficacy and safety of TAS-116, an oral inhibitor of heat shock protein 90, in patients with metastatic or unresectable gastrointestinal stromal tumour refractory to imatinib, sunitinib and regorafenib: a phase II, single-arm trial, Eur. J. Cancer 121 (2019) 29–39, https://doi.org/10.1016/j.ejca.2019.08.009.
[4] M.N. Wente, M.W. Büchler, J. Weitz, Gastrointestinal stromal tumors (GIST), Surg. Therapy Chirurg. 79 (2008) 638–643, https://doi.org/10.1007/s00104-008-1527-5.
[5] B.D. Smith, M.D. Kaufman, W.P. Lu, A. Gupta, C.B. Leary, S.C. Wise, T.J. Rutkoski, Y.M. Ahn, G. Al-Ani, S.L. Bulfer, T.M. Caldwell, L. Chun, C.L. Ensinger, M.M. Hood, A. McKinley, W.C. Patt, R. Ruiz-Soto, Y. Su, H. Telikepalli, A. Town, B.A. Turner, L. Vogeti, S. Vogeti, K. Yates, F. Janku, A.R. Abdul Razak, O. Rosen, M.C. Heinrich, D.L. Flynn, Ripretinib (DCC-2618)is a switch control kinase inhibitor of a broad spectrum of oncogenic and drug-resistant KIT and PDGFRA variants, Cancer Cell 35 (2019) 738–751.e9, https://doi.org/10.1016/j.ccell.2019.04.006.
[6] M.T. Villanueva, Ripretinib turns off the switch in GIST, Nat. Rev. Cancer 19 (2019) 370, https://doi.org/10.1038/s41568-019-0167-z.
[7] C. Yoo, Y. Mi Ryu, S.Y. Kim, J. Kim, C.Y. Ock, M.H. Ryu, Y.K. Kang, Association between the exposure to anti-angiogenic agents and tumour immune microenvironment in advanced gastrointestinal stromal tumours, Br. J. Cancer 121 (2019) 819–826, https://doi.org/10.1038/s41416-019-0596-1.
[8] M. von Mehren, C. Serrano, S. Bauer, H. Gelderblom, S. George, M. Heinrich, P. Schöffski, J. Zalcberg, P. Chi, R.L. Jones, P. Reichardt, S. Attia, G. D'Amato, J. Meade, K. Shi, R. Ruiz-Soto, J.-Y. Blay, INVICTUS: A phase III, interventional, double-blind, placebo-controlled study to assess the safety and efficacy of ripretinib as ≥ 4th-line therapy in patients with advanced gastrointestinal stromal tumors (GIST) who have received treatment with prior ant, Ann. Oncol. 30 (2019) v925–v926, https://doi.org/10.1093/annonc/mdz394.087.
[9] J.-Y. Blay, C. Serrano, M.C. Heinrich, J. Zalcberg, S. Bauer, H. Gelderblom, P. Schöffski, R.L. Jones, S. Attia, G. D'Amato, P. Chi, P. Reichardt, J. Meade, K. Shi, R. Ruiz-Soto, S. George, M. von Mehren, Ripretinib in patients with advanced gastrointestinal stromal tumours (INVICTUS): a double-blind, randomised, placebo-controlled, phase 3 trial, Lancet Oncol. 2045 (2020) 1–12, https://doi.org/10.1016/s1470-2045(20)30168-6.
[10] K.-S. Yuen, Z.-W. Ye, S.-Y. Fung, C.-P. Chan, D.-Y. Jin, SARS-CoV-2 and COVID-19: the most important research questions, Cell Biosci. 10 (2020) 40, https://doi.org/10.1186/s13578-020-00404-4.
[11] Z. Xu, L. Shi, Y. Wang, J. Zhang, L. Huang, C. Zhang, S. Liu, P. Zhao, H. Liu, L. Zhu, Y. Tai, C. Bai, T. Gao, J. Song, P. Xia, J. Dong, J. Zhao, F.-S. Wang, Pathological findings of COVID-19 associated with acute respiratory distress syndrome, Lancet Respir. Med. 8 (2020) 420–422, https://doi.org/10.1016/S2213-2600(20)30076-X.
[12] M.A. Lake, What we know so far: COVID-19 current clinical knowledge and research, Clin. Med. 20 (2020) 124–127, https://doi.org/10.7861/clinmed.2019-coron.
[13] F. Touret, X. de Lamballerie, Of chloroquine and COVID-19, Antivir. Res. 177 (2020) 104762, https://doi.org/10.1016/j.antiviral.2020.104762.
[14] Y. Wang, D. Zhang, G. Du, R. Du, J. Zhao, Y. Jin, S. Fu, L. Gao, Z. Cheng, Q. Lu, Y. Hu, G. Luo, K. Wang, Y. Lu, H. Li, S. Wang, S. Ruan, C. Yang, C. Mei, Y. Wang, D. Ding, F. Wu, X. Tang, X. Ye, Y. Ye, B. Liu, J. Yang, W. Yin, A. Wang, G. Fan, F. Zhou, Z. Liu, X. Gu, J. Xu, L. Shang, Y. Zhang, L. Cao, T. Guo, Y. Wan, H. Qin, Y. Jiang, T. Jaki, F.G. Hayden, P.W. Horby, B. Cao, C. Wang, Remdesivir in adults with severe COVID-19: a randomised, double-blind, placebo-controlled, multicentre trial, Lancet 395 (2020) 1569–1578, https://doi.org/10.1016/S0140-6736(20)31022-9.
[15] R. Wu, L. Wang, H.-C.D. Kuo, A. Shannar, R. Peter, P.J. Chou, S. Li, R. Hudlikar, X. Liu, Z. Liu, G.J. Poiani, L. Amorosa, L. Brunetti, A.-N. Kong, An update on current therapeutic drugs treating COVID-19, Curr. Pharmacol. Reports. 6 (2020) 56–70, https://doi.org/10.1007/s40495-020-00216-7.
[16] N. Al-Zaqri, T. Pooventhiran, A. Alsalme, I. Warad, A.M. John, R. Thomas, Structural and physico-chemical evaluation of melatonin and its solution-state excited properties, with emphasis on its binding with novel coronavirus proteins, J. Mol. Liq. 318 (2020) 114082, https://doi.org/10.1016/j.molliq.2020.114082.
[17] A. Alsalme, T. Pooventhiran, N. Al-Zaqri, D.J. Rao, S.S. Rao, R. Thomas, Modelling the structural and reactivity landscapes of tucatinib with special reference to its wavefunction-dependent properties and screening for potential antiviral activity, J. Mol. Model. 26 (2020) 341, https://doi.org/10.1007/s00894-020-04603-1.
[18] Z. Ullah, R. Thomas, Mechanistic insights can resolve the low reactivity and selectivity issues in intermolecular Rauhut–Currier (RC) reaction of γ-hydroxyenone, New J. Chem. 44 (2020) 12857–12865, https://doi.org/10.1039/D0NJ02732D.
[19] D.J.F.M.J. Frisch, G.W. Trucks, H.B. Schlegel, G.E. Scuseria, M.A. Robb, J.R. Cheeseman, G. Scalmani, V. Barone, G.A. Petersson, H. Nakatsuji, X. Li, M. Caricato, A. Marenich, J. Bloino, B.G. Janesko, R. Gomperts, B. Mennucci, H.P. Hratchian, J.V. Ort, Gaussian09W Revision D.01, 2009.
[20] M. Orio, D.A. Pantazis, F. Neese, Density functional theory, Photosynth. Res. 102 (2009) 443–453, https://doi.org/10.1007/s11120-009-9404-8.
[21] P.J. Stephens, F.J. Devlin, C.F. Chabalowski, M.J. Frisch, Ab initio calculation of vibrational absorption and circular Dichroism spectra using density functional force fields, J. Phys. Chem. 98 (1994) 11623–11627, https://doi.org/10.1021/j100096a001.
[22] S.H. Vosko, L. Wilk, M. Nusair, Accurate spin-dependent electron liquid correlation energies for local spin density calculations: a critical analysis, Can. J. Phys. 58 (1980) 1200–1211, https://doi.org/10.1139/p80-159.
[23] C. Lee, W. Yang, R.G. Parr, Development of the Colle-Salvetti correlation-energy formula into a functional of the electron density, Phys. Rev. B 37 (1988) 785–789, https://doi.org/10.1103/PhysRevB.37.785.
[24] P.J. Hay, W.R. Wadt, Ab initio effective core potentials for molecular calculations. Potentials for the transition metal atoms Sc to Hg, J. Chem. Phys. 82 (1985) 270–283, https://doi.org/10.1063/1.448799.
[25] J.B. Foresman, Ae. Frisch, I. Gaussian, Exploring Chemistry With Electronic Structure Methods, Gaussian, Inc, 1996.
[26] T. Yanai, D.P. Tew, N.C. Handy, A new hybrid exchange–correlation functional using the coulomb-attenuating method (CAM-B3LYP), Chem. Phys. Lett. 393 (2004) 51–57, https://doi.org/10.1016/J.CPLETT.2004.06.011.
[27] K. Okuno, Y. Shigeta, R. Kishi, H. Miyasaka, M. Nakano, Tuned CAM-B3LYP functional in the time-dependent density functional theory scheme for excitation energies and properties of diarylethene derivatives, J. Photochem. Photobiol. A Chem. 235 (2012) 29–34, https://doi.org/10.1016/j.jphotochem.2012.03.003.
[28] M. Cossi, V. Barone, R. Cammi, J. Tomasi, Ab initio study of solvated molecules: a new implementation of the polarizable continuum model, Chem. Phys. Lett. 255 (1996) 327–335, https://doi.org/10.1016/0009-2614(96)00349-1.
[29] K.E. Srikanth, A. Veeraiah, T. Pooventhiran, R. Thomas, K.A. Solomon, C.J.S. Raju, J.N.L. Latha, Detailed molecular structure (XRD), conformational search, spectroscopic characterization (IR, Raman, UV, fluorescence), quantum mechanical properties and bioactivity prediction of a pyrrole analogue, Heliyon. 6 (2020), e04106, .
[30] N.M. O'boyle, A.L. Tenderholt, K.M. Langner, CCLIB: a library for package-independent computational chemistry algorithms, J. Comput. Chem. 29 (2008) 839–845, https://doi.org/10.1002/jcc.20823.
[31] T. Lu, F. Chen, Multiwfn: a multifunctional wavefunction analyzer, J. Comput. Chem. 33 (2012) 580–592, https://doi.org/10.1002/jcc.22885.
[32] E.R. Johnson, S. Keinan, P. Mori-Sánchez, J. Contreras-García, A.J. Cohen, W. Yang, Revealing noncovalent interactions, J. Am. Chem. Soc. 132 (2010) 6498–6506, https://doi.org/10.1021/ja100936w.
[33] S.K. Burley, H.M. Berman, C. Bhikadiya, C. Bi, L. Chen, L. Di Costanzo, C. Christie, K. Dalenberg, J.M. Duarte, S. Dutta, Z. Feng, S. Ghosh, D.S. Goodsell, R.K. Green, V. Guranović, D. Guzenko, B.P. Hudson, T. Kalro, Y. Liang, R. Lowe, H. Namkoong, E. Peisach, I. Periskova, A. Prlić, C. Randle, A. Rose, P. Rose, R. Sala, M. Sekharan, C. Shao, L. Tan, Y.-P. Tao, Y. Valasatava, M. Voigt, J. Westbrook, J. Woo, H. Yang, J. Young, M. Zhuravleva, C. Zardecki, RCSB Protein Data Bank: biological macromolecular structures enabling research and education in fundamental biology, biomedicine, biotechnology and energy, Nucleic Acids Res. 47 (2018) D464–D474, https://doi.org/10.1093/nar/gky1004.
[34] D. Schneidman-Duhovny, Y. Inbar, R. Nussinov, H.J. Wolfson, PatchDock and SymmDock: servers for rigid and symmetric docking, Nucleic Acids Res. 33 (2005) W363–W367, https://doi.org/10.1093/nar/gki481.
[35] P. Politzer, P.R. Laurence, K. Jayasuriya, Molecular electrostatic potentials: an effective tool for the elucidation of biochemical phenomena, Environ. Health Perspect. 61 (1985) 191–202, https://doi.org/10.1289/ehp.8561191.
[36] J.S. Al-Otaibi, Y.S. Mary, Y.S. Mary, R. Thomas, Quantum mechanical and photovoltaic studies on the cocrystals of hydrochlorothiazide with isonazid and malonamide, J. Mol. Struct. 1197 (2019) 719–726, https://doi.org/10.1016/j.molstruc.2019.07.110.
[37] J.S. Al-Otaibi, Y. Sheena Mary, Y. Shyma Mary, C.Y. Panicker, R. Thomas, Cocrystals of pyrazinamide with p-toluenesulfonic and ferulic acids: DFT investigations and molecular docking studies, J. Mol. Struct. 1175 (2019) 916–926, https://doi.org/10.1016/j.molstruc.2018.08.055.
[38] R. Thomas, Y.S. Mary, K.S. Resmi, B. Narayana, B.K. Sarojini, G. Vijayakumar, C. Van Alsenoy, Two neoteric pyrazole compounds as potential anti-cancer agents: synthesis, electronic structure, physico-chemical properties and docking analysis, J. Mol. Struct. 1181 (2019) 455–466, https://doi.org/10.1016/j.molstruc.2019.01.003.

[39] A.M. John, J. Jose, R. Thomas, K.J. Thomas, S.P. Balakrishnan, Spectroscopic and TDDFT investigation of highly selective fluoride sensors by substituted acyl hydrazones, Spectrochim. Acta Part A Mol. Biomol. Spectrosc. (2020), 118329, https://doi.org/10.1016/j.saa.2020.118329.

[40] A.M. John, R. Thomas, S.P. Balakrishnan, N. Al-Zaqri, A. Alsalme, I. Warad, Diazopyrazole analogues as photosensitizers in dye sensitised solar cells: tuning for a better photovoltaic efficiency using a new modelling strategy using experimental and computational data, Zeitschrift Für Phys. Chemie. (2020)https://doi.org/10.1515/zpch-2020-1722.

[41] P.K. Chattaraj, S. Giri, Electrophilicity index within a conceptual DFT framework, Annu. Rep. Prog. Chem. Sect. C Phys. Chem. 105 (2009) 13–39https://doi.org/10.1039/B802832J.

[42] P.K. Chattaraj, U. Sarkar, D.R. Roy, Electrophilicity index, Chem. Rev. 106 (2006) 2065–2091, https://doi.org/10.1021/cr040109f.

[43] L.R. Domingo, M. Ríos-Gutiérrez, P. Pérez, Applications of the conceptual density functional theory indices to organic chemistry reactivity, Molecules. 21 (2016) 748, https://doi.org/10.3390/molecules21060748.

[44] P. Politzer, J.S. Murray, An Occam's razor approach to chemical hardness: lex parsimoniae, J. Mol. Model. 24 (2018) 332, https://doi.org/10.1007/s00894-018-3864-8.

[45] J.S. Al-Otaibi, Y.S. Mary, R. Thomas, B. Narayana, Theoretical studies into the spectral characteristics, biological activity, and photovoltaic cell efficiency of four new polycyclic aromatic Chalcones, Polycycl. Aromat. Compd. (2020) 1–15, https://doi.org/10.1080/10406638.2020.1747097.

[46] D.A. Thadathil, S. Varghese, K.B. Akshaya, R. Thomas, A. Varghese, An insight into photophysical investigation of (E)-2-Fluoro-N'-(1-(4-Nitrophenyl) ethylidene) benzohydrazide through solvatochromism approaches and computational studies, J. Fluoresc. 29 (2019) 1013–1027.

[47] T. Sajini, R. Thomas, B. Mathew, Rational design and synthesis of photo-responsive molecularly imprinted polymers for the enantioselective intake and release of L-phenylalanine benzyl ester on multiwalled carbon nanotubes, Polym. (Guildf). 173 (2019) 127–140.

[48] D. Majumdar, S. Das, R. Thomas, Z. Ullah, S.S. Sreejith, D. Das, P. Shukla, K. Bankura, D. Mishra, Syntheses, X-ray crystal structures of two new Zn (II)-dicyanamide complexes derived from H2vanen-type compartmental ligands: investigation of thermal, photoluminescence, in vitro cytotoxic effect and DFT-TDDFT studies, Inorg. Chim. Acta 492 (2019) 221–234.

[49] Y.S. Mary, Y.S. Mary, K.S. Resmi, V.S. Kumar, R. Thomas, B. Sureshkumar, Detailed quantum mechanical, molecular docking, QSAR prediction, photovoltaic light harvesting efficiency analysis of benzil and its halogenated analogues, Heliyon. 5 (2019), e02825, https://doi.org/10.1016/j.heliyon.2019.e02825.

[50] Y.S. Mary, G. Yalcin, Y.S. Mary, K.S. Resmi, R. Thomas, T. Önkol, E.N. Kasap, I. Yildiz, Spectroscopic, quantum mechanical studies, ligand protein interactions and photovoltaic efficiency modeling of some bioactive benzothiazolinone acetamide analogs, Chem. Pap. (2020)https://doi.org/10.1007/s11696-019-01047-7.

[51] M. Hossain, R. Thomas, Y.S. Mary, K.S. Resmi, S. Armaković, S.J. Armaković, A.K. Nanda, G. Vijayakumar, C. Van Alsenoy, Understanding reactivity of two newly synthetized imidazole derivatives by spectroscopic characterization and computational study, J. Mol. Struct. 1158 (2018) 176–196, https://doi.org/10.1016/j.molstruc.2018.01.029.

[52] P. Kavitha Rani, Y. Sheena Mary, A. Fernandez, Y.S. Mary, R. Thomas, Single crystal XRD, DFT investigations and molecular docking study of 2-((1, 5-dimethyl-3-oxo-2-phenyl-2, 3-dihydro-1H-pyrazol-4-yl) amino) naphthalene-1, 4-dione as a potential anti-cancer lead molecule, Comput. Biol. Chem. 78 (2019) 153–164.

[53] Y.S. Mary, Y.S. Mary, R. Thomas, B. Narayana, S. Samshuddin, B.K. Sarojini, S. Armaković, S.J. Armaković, G.G. Pillai, Theoretical studies on the structure and various Physico-chemical and biological properties of a Terphenyl derivative with immense anti-protozoan activity, Polycycl. Aromat. Compd. (2019)https://doi.org/10.1080/10406638.2019.1624974 (In Press).

[54] R. Thomas, Y.S. Mary, K.S. Resmi, B. Narayana, B.K. Sarojini, G. Vijayakumar, C. Van Alsenoy, Two neoteric pyrazole compounds as potential anti-cancer agents: synthesis, electronic structure, physico-chemical properties and docking analysis, J. Mol. Struct. 1181 (2019) 455–466.

[55] S. Jeeva, S. Muthu, R. Thomas, B.R. Raajaraman, G. Mani, G. Vinitha, Co-crystals of urea and hexanedioic acid with third-order nonlinear properties: an experimental and theoretical enquiry, J. Mol. Struct. 1202 (2020) 127237, https://doi.org/10.1016/j.molstruc.2019.127237.

[56] J.S. Al-Otaibi, Y.S. Mary, S. Armaković, R. Thomas, Hybrid and bioactive cocrystals of pyrazinamide with hydroxybenzoic acids: detailed study of structure, spectroscopic characteristics, other potential applications and noncovalent interactions using SAPT, J. Mol. Struct. 1202 (2020) 127316, https://doi.org/10.1016/j.molstruc.2019.127316.

[57] Y.S. Mary, P.B. Miniyar, Y.S. Mary, K.S. Resmi, C.Y. Panicker, S. Armaković, S.J. Armaković, R. Thomas, B. Sureshkumar, Synthesis and spectroscopic study of three new oxadiazole derivatives with detailed computational evaluation of their reactivity and pharmaceutical potential, J. Mol. Struct. 1173 (2018) 469–480, https://doi.org/10.1016/j.molstruc.2018.07.026.

[58] R. Thomas, Y.S. Mary, K.S. Resmi, B. Narayana, S.B.K. Sarojini, S. Armaković, S.J. Armaković, G. Vijayakumar, C. Van Alsenoy, B.J. Mohan, Synthesis and spectroscopic study of two new pyrazole derivatives with detailed computational evaluation of their reactivity and pharmaceutical potential, J. Mol. Struct. 1181 (2019) 599–612, https://doi.org/10.1016/j.molstruc.2019.01.014.

[59] A. Matondo, R. Thomas, P.V. Tsalu, C.T. Mukeba, V. Mudogo, α-methylation and α-fluorination electronic effects on the regioselectivity of carbonyl groups of uracil by H and triel bonds in the interaction of U, T and 5FU with HCl and TrH 3 (Tr = B, Al), J. Mol. Graph. Model. 88 (2019) 237–246, https://doi.org/10.1016/j.jmgm.2019.02.006.

[60] F. Weinhold, Natural bond orbital analysis: a critical overview of relationships to alternative bonding perspectives, J. Comput. Chem. 33 (2012) 2363–2379, https://doi.org/10.1002/jcc.23060.

[61] K. Haruna, V.S. Kumar, Y. Sheena Mary, S.A. Popoola, R. Thomas, M.S. Roxy, A.A. Al-Saadi, Conformational profile, vibrational assignments, NLO properties and molecular docking of biologically active herbicide1,1-dimethyl-3-phenylurea, Heliyon. 5 (2019), e01987, https://doi.org/10.1016/j.heliyon.2019.e01987.

[62] E. D. Glendening, A.E. Reed, J.E. Carpenter, F. Weinhold, NBO Version 3.1, (2003).

[63] P. Politzer, J.S. Murray, Molecular electrostatic potentials and chemical reactivity, Rev. Comput. Chem. (1991) 273–312, https://doi.org/10.1002/9780470125793.ch7.

[64] P. Politzer, J.S. Murray, The fundamental nature and role of the electrostatic potential in atoms and molecules, Theor. Chem. Accounts 108 (2002) 134–142, https://doi.org/10.1007/s00214-002-0363-9.

[65] P. Politzer, J.S. Murray, F.A. Bulat, Average local ionization energy: a review, J. Mol. Model. 16 (2010) 1731–1742, https://doi.org/10.1007/s00894-010-0709-5.

[66] RCSB PDB - 6M03: The crystal structure of COVID-19 main protease in apo form, https://www.rcsb.org/structure/6M03 2020 (accessed July 6, 2020).